



Geophysical Research Letters®

RESEARCH LETTER

10.1029/2025GL116478

Key Points:

- We quantify the differential energy flux of electron precipitation driven by chorus waves through self-consistent PIC simulations
- Self-consistent simulations using magnetospheric plasma parameters show significant differences from test particle simulation results
- The dependence of precipitation intensity on the number density and temperature anisotropy of energetic electrons is established

Supporting Information:

Supporting Information may be found in the online version of this article.

Correspondence to:

H. Chen and X. Wang,
huayue_chen@foxmail.com;
wangxue@auburn.edu

Citation:

Chen, H., Wang, X., Li, X., Chen, R., Chen, L., Omura, Y., et al. (2025). Quantifying electron precipitation driven by chorus waves using self-consistent particle-in-cell simulations. *Geophysical Research Letters*, 52, e2025GL116478. <https://doi.org/10.1029/2025GL116478>

Received 19 APR 2025

Accepted 28 SEP 2025

Quantifying Electron Precipitation Driven by Chorus Waves Using Self-Consistent Particle-In-Cell Simulations

Huayue Chen¹ , Xueyi Wang¹ , Xiaolei Li¹ , Rui Chen¹ , Lunjin Chen² , Yoshiharu Omura³ , Yi-Kai Hsieh³ , Yu Lin¹ , and M. L. Adrian¹

¹Department of Physics, Auburn University, Auburn, AL, USA, ²William B. Hanson Center for Space Sciences, University of Texas at Dallas, Richardson, TX, USA, ³Research Institute for Sustainable Humanosphere, Kyoto University, Kyoto, Japan

Abstract The precipitation of tens to hundreds of keV electrons from Earth's magnetosphere plays a crucial role in magnetosphere-ionosphere coupling, primarily driven by chorus wave scattering. Most existing simulations of electron precipitation rely on test particle models that neglect particle feedback on waves. However, both theoretical and observational studies indicate that the feedback from energetic electrons significantly influences chorus wave excitation and evolution. In this study, we quantify electron precipitation driven by chorus waves using self-consistent simulations at $L = 6$ with typical magnetospheric plasma parameters. Electrons in the $\sim 10\text{--}200$ keV range are precipitated, exhibiting energy-dispersive characteristics. The precipitation intensity reaches $\sim 10^8\text{--}10^9$ keV/s/sr/cm 2 /MeV, consistent with the typical values in observations. As a comparison, test particle simulations underestimate the precipitation intensity by nearly an order of magnitude. These results highlight the importance of self-consistent simulations in quantifying electron precipitation and investigating wave-particle interactions that modulate magnetospheric dynamics.

Plain Language Summary Energetic electron fluxes in the Earth's magnetosphere vary significantly during geomagnetic periods, controlled by the relative balance among acceleration, transport, and loss processes. A major loss mechanism is the precipitation of tens to hundreds of keV electrons driven by chorus wave scattering. Numerical simulations are commonly used to study this process. Most previous simulations rely on test particle models that neglect the feedback from particles to waves, despite the crucial role of tens of keV electrons in chorus wave generation. In this study, we quantify electron precipitation under typical magnetospheric parameters using a self-consistent model, in which chorus wave excitation, propagation, and particle scattering are determined by fully-coupled wave-particle interactions. It is found that electrons in the $\sim 10\text{--}200$ keV range are precipitated, producing an energy-dispersive precipitation pattern with the intensity comparable with satellite observations. As a comparison, test particle simulations underestimate the precipitation intensity by an order of magnitude. The results demonstrate the importance of self-consistent wave-particle interactions in quantifying chorus-driven electron precipitation.

1. Introduction

The precipitation of tens to hundreds of keV electrons is a major loss mechanism for energetic electrons in the Earth's magnetosphere, primarily driven by chorus wave scattering (Artemyev et al., 2022; Jaynes et al., 2015; Miyoshi et al., 2020; Ozaki et al., 2019; Shen et al., 2023; Summers et al., 2007; Tsurutani et al., 2013). Due to its characteristic millisecond timescale, this precipitation is also referred to as electron microbursts (Anderson & Milton, 1964; Hikishima et al., 2010; Kang et al., 2022; Tsurutani et al., 2013; Zhang et al., 2022). The precipitating electrons travel along magnetic field lines to the upper ionosphere, where they generate pulsating aurora (R. Chen et al., 2024; Gao et al., 2023; Kasahara et al., 2018; Miyoshi et al., 2015; Ozaki et al., 2019). Therefore, electron precipitation serves as a key energy source for the ionosphere and plays a crucial role in magnetosphere-ionosphere coupling (Khazanov et al., 2018; Lyons, 1992; Zhang et al., 2015).

Chorus waves are coherent electromagnetic emissions characterized by a rising-tone chirping spectrum (Burtis & Helliwell, 1969; Tsurutani & Smith, 1974), with their spectrum showing a one-to-one relationship with electron precipitation (Breneman et al., 2017; H. Chen et al., 2025; Kasahara et al., 2018; Miyoshi et al., 2015; Ozaki et al., 2018; Tsurutani et al., 2013). Numerical simulations are widely used to quantify electron precipitation driven by chorus waves. Most existing simulations rely on test particle (TP) models (Bortnik et al., 2008; L. Chen et al., 2020; Gan et al., 2020; O'Brian et al., 2022), in which wave evolution is prescribed, and particle

© 2025 The Author(s).

This is an open access article under the terms of the Creative Commons Attribution-NonCommercial License, which permits use, distribution and reproduction in any medium, provided the original work is properly cited and is not used for commercial purposes.

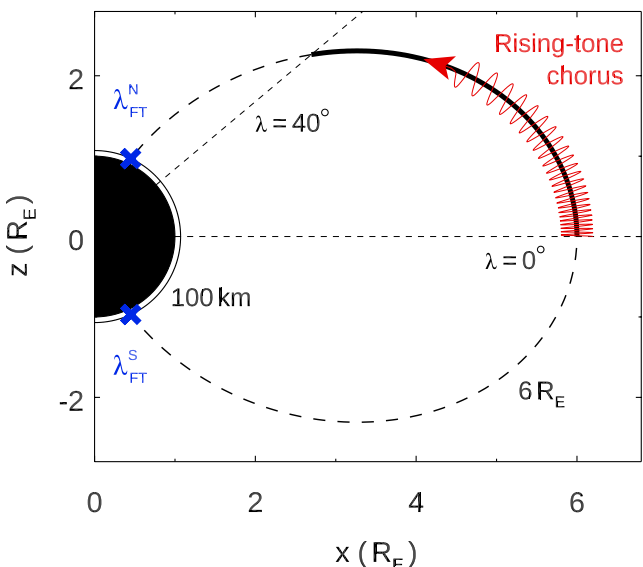


Figure 1. Schematic plot of the simulation domain in the meridian plane. The dashed line represents the magnetic field line at $L = 6$, with the magnetic footprints λ_{FT}^N and λ_{FT}^S (blue crosses) marking the upper ionosphere, located 100 km above Earth's surface in the northern and southern hemispheres, respectively. The thick black curve from $\lambda = 0^\circ$ to 40° outlines the simulation domain. Rising-tone chorus waves, shown as red wave cycles, are injected from the magnetic equator.

gorithm is used (H. Chen, Wang, Chen, Omura, Lu, et al., 2023; Lu et al., 2021). Absorbing boundary conditions are applied to fields, and reflecting boundary conditions are imposed on particles.

Figure 1 shows a schematic illustration of the simulation domain (thick black curve). To save computational resources, simulations are performed in a reduced system with a scaling factor of 10 at $L = 6$ (Ke et al., 2022). Further details are provided in Supporting Information S1. Typical plasma parameters at $L \sim 6$ are adopted. The domain consists of 4,000 grid cells and spans a magnetic latitude range from $\lambda = 0^\circ$ to $\sim 40^\circ$. The black dashed curves represent the background magnetic field line, with λ_{FT}^N and λ_{FT}^S (blue crosses) indicating the magnetic footprints at an altitude of 100 km (corresponding to $1.016 R_E$, where R_E is the Earth radius) in the northern and southern hemispheres, respectively. At the northern and southern boundaries of the simulation domain, electrons that enter the loss cone are removed and recorded as precipitating electrons. When calculating precipitating flux, the adiabatic motion of electrons from boundaries to the upper ionosphere (~ 100 km) is considered, including the effect of magnetic field convergence. The flux is collected at the upper ionosphere rather than at the simulation boundaries.

The equatorial background magnetic field is $B_{e0} = 144.4 \text{ nT}$, corresponding to the dipole field strength at $L = 6$ (i.e., $31,200 \text{ nT}/6^3$). The plasma density is $n_{e0} = 5.0 \text{ cm}^{-3}$ (Fu et al., 2014; Macúšová et al., 2010), yielding a ratio between the electron plasma frequency and the equatorial electron gyrofrequency of $\omega_{pe}/\Omega_{e0} = 4.98$, where $\omega_{pe} = \sqrt{n_{e0}e^2/m_e\varepsilon_0}$ and $\Omega_{e0} = eB_{e0}/m_e$. Here, e is the elementary charge, m_e is the electron mass, and ε_0 is the vacuum permittivity. The plasma system consists of energetic electrons, background electrons, and immobile protons. The energetic electrons at the magnetic equator follow a subtracted Maxwellian distribution (H. Chen, Wang, Chen, Omura, Tsurutani, et al., 2023; Omura, 2021), with details provided in Supporting Information S1. Typical parameters for energetic electrons at $L \sim 6$ include a temperature of $\sim 10\text{--}20 \text{ keV}$ (Li, Thorne, et al., 2011; Li, Bortnik, et al., 2011), a temperature anisotropy of ~ 2 (Fu et al., 2014; Yue et al., 2016), and a number density of $\sim 10^{-3}\text{--}10^{-2}n_{e0}$ (Gao et al., 2014; Li, Bortnik, et al., 2011). During active geomagnetic periods, the number density even increases to $\sim 10^{-1}n_{e0}$ (R. Chen et al., 2019; Fu et al., 2014; Li, Thorne, et al., 2011). Based on these observations, we set the parallel temperature of energetic electrons in the simulation to $T_{||} = 20 \text{ keV}$. Six groups of temperature anisotropy are considered: $T_{\perp}/T_{||} = 1.25, 1.50, 1.75, 2.00, 2.25$, and 2.50 . Additionally, five groups of

feedback on waves is neglected. Nevertheless, both theoretical and observational studies indicate that tens of keV electrons play an important role in chorus wave excitation and evolution (Hikishima et al., 2010; Horne & Thorne, 1998; Li, Thorne, et al., 2011; Li, Bortnik, et al., 2011; Summers et al., 2007; Lu et al., 2019; Wang et al., 2024). To comprehensively address the physics in electron precipitation, self-consistent (SC) simulations are required, where wave excitation, propagation, and electron scattering are determined by fully-coupled wave-particle interactions.

In this study, we quantify electron precipitation driven by chorus waves using SC simulations with the typical plasma parameters derived from observations and compare the results with those from TP simulations. In SC simulations, the feedback from energetic electrons contributes to wave growth, which in turn enhances electron precipitation intensity. The resulting differential energy flux reaches $\sim 10^8\text{--}10^9 \text{ keV/s/sr/cm}^2/\text{MeV}$, comparable with the observations from low Earth orbit (LEO) satellites. In contrast, TP simulations underestimate the precipitation intensity by nearly an order of magnitude.

2. Simulation Model

We perform one-dimensional (1-D) particle-in-cell simulations using the general curvilinear plasma simulation code (GCPIC) model to investigate electron precipitation driven by parallel chorus waves (H. Chen et al., 2025; Kong et al., 2025; Wang et al., 2024). A dipole magnetic field in the meridian plane is used as the background field. Particle trajectories are calculated by advancing their three-dimensional (3-D) velocities and positions. The δf al-

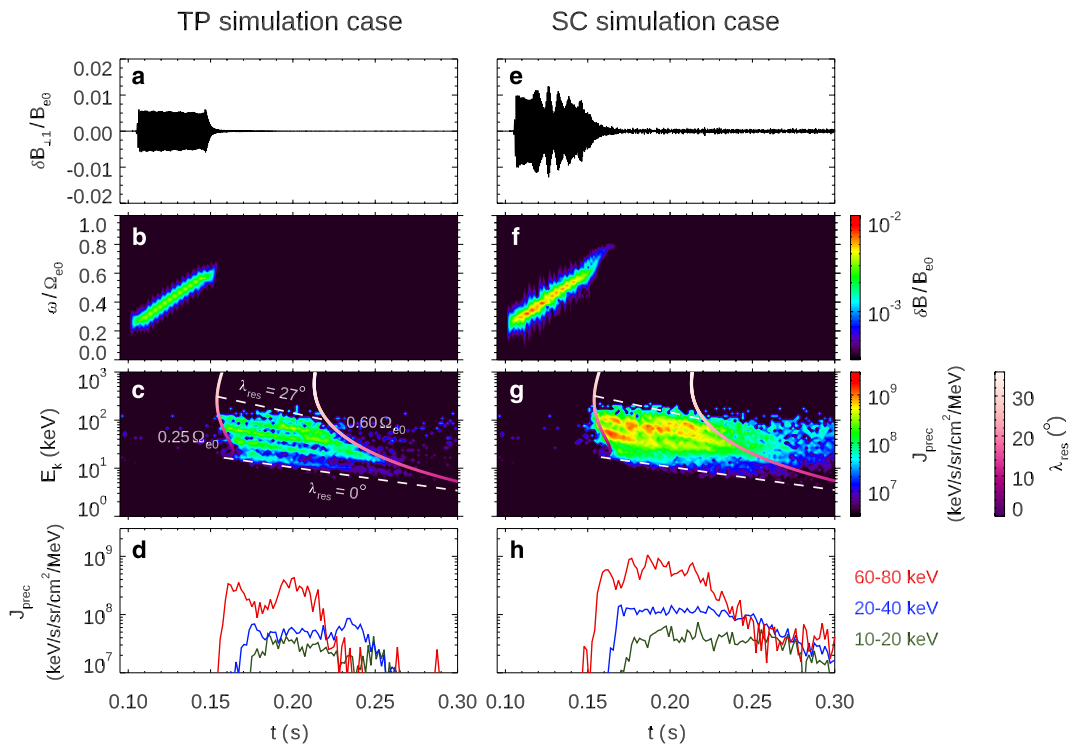


Figure 2. Comparison between the TP and SC simulations with $n_{\text{heq}}/n_{e0} = 0.010$ and $T_{\perp}/T_{\parallel} = 1.50$ for energetic electrons. (a, e) Waveform and (b, f) spectrum for chorus wave $\delta B/B_{e0}$ at $\lambda = 5^\circ$. (c, g) Differential energy flux of precipitating electrons J_{prec} at λ_{FFT}^S . Solid curves indicate the theoretical correlation between E_{res} and t_{prec} for wave frequencies of $0.25 \Omega_{e0}$ and $0.60 \Omega_{e0}$, with color coding indicating λ_{res} . White dashed lines denote $\lambda_{\text{res}} = 0^\circ$ and $\lambda_{\text{res}} = 27^\circ$, determined by fitting the boundaries of the differential energy flux. (d, h) Temporal evolution of the average precipitation intensity J_{prec} for different E_k ranges: 60–80 keV (red), 20–40 keV (blue), and 10–20 keV (green). The left column corresponds to the TP case, and the right column corresponds to the SC case.

equatorial number density are examined: $n_{\text{heq}}/n_{e0} = 0.003, 0.005, 0.010, 0.017$, and 0.030 . Other parameters along the field line are derived using Liouville's theorem. The particle number per cell (ppc) is set to 4,000. The background electrons are treated as a cold fluid.

Rising-tone chorus waves are injected from the magnetic equator (red wave cycles in Figure 1), with their frequency ω increasing from $0.25 \Omega_{e0}$ to $0.60 \Omega_{e0}$ over ~ 0.04 s (equivalent to $1000 \Omega_{e0}^{-1}$). The wave amplitude is $\delta B/B_{e0} \sim 0.005$ (Gao et al., 2014). To remove particles inside the loss cone at the initial stage, waves are injected after ~ 0.1 s (equivalent to $2500 \Omega_{e0}^{-1}$). Electron precipitation is quantified using SC simulations, and TP simulations are also performed for comparison.

3. Simulation Results

3.1. Typical Cases

We present two typical cases from TP and SC simulations using energetic electrons with $n_{\text{heq}}/n_{e0} = 0.010$ and $T_{\perp}/T_{\parallel} = 1.50$. Figures 2a and 2b show the waveform of $\delta B_{\perp1}/B_{e0}$ and the spectrum of $\delta B/B_{e0}$ for chorus waves at $\lambda = 5^\circ$ in the TP case, respectively. Here, $\delta B = \sqrt{\delta B_{\perp1}^2 + \delta B_{\perp2}^2}$ (“ \perp ” refers to the radial direction, and “ $\perp\perp$ ” refers to the azimuthal direction) is the wave amplitude, which remains constant during propagation. We focus on the electron scattering driven by cyclotron resonance, in which resonant electrons counter-propagate with waves. Figure 2c presents the differential energy flux of precipitating electrons, J_{prec} , collected at λ_{FFT}^S . Precipitation occurs within the energy range of $E_k \sim 10$ –200 keV, with a peak intensity of $\sim 10^8$ keV/s/sr/cm 2 /MeV. Higher-energy electrons precipitate earlier, while lower-energy electrons arrive later, resulting in energy-dispersive precipitation. This is further illustrated by the line plots in Figure 2d, which show the average intensity across

different energy ranges as a function of time. The precipitation of electrons ranging from tens to hundreds of keV, along with an energy-dispersive pattern, is also observed by LEO satellites (Miyoshi et al., 2015; Mozer et al., 2018; Zhang et al., 2022).

A time delay exists between the wave and precipitation signals due to their measurements at different latitudes. The theoretical precipitation time t_{prec} , which depends on both wave frequency and the kinetic energy of precipitating electrons, is evaluated using the time-of-flight analysis based on the Miyoshi-Saito model (Miyoshi et al., 2010; Saito et al., 2012):

$$t_{\text{prec}} = t_L(\omega) + \int_0^{h(\lambda_{\text{res}})} \frac{dh}{v_g(\omega, h)} + \int_{h(\lambda_{\text{res}})}^{h(\lambda_{\text{FT}}^S)} \frac{dh}{v_{\text{res}}(\omega, h)}, \quad (1)$$

where $t_L(\omega)$ is the launch time of chorus waves, h is the distance along the field line to the magnetic equator, λ_{res} is the magnetic latitude at which the resonant interaction occurs, v_g is the wave group velocity, and v_{res} is the electron resonant velocity. The cyclotron resonance condition is given by

$$\omega - k(h) v_{\text{res}}(h) = \frac{\Omega_e(h)}{\gamma}, \quad (2)$$

where $k(h)$ is the wave number, $\Omega_e(h) = eB_0(h)/m_e$ is the local electron gyrofrequency, $B_0(h)$ is the local background magnetic field, and γ is the Lorentz factor. The loss cone angle at the magnetic equator is given by

$$\alpha_{lc} = \sin^{-1} \left[\sin(\alpha(h)) \sqrt{\frac{B_{e0}}{B_0(h)}} \right], \quad (3)$$

with α being the pitch angle at a distance h . The resonant energy E_{res} of precipitating electrons is estimated from Equations 2 and 3.

The thick curves with a magenta-to-white gradient in Figure 2c illustrate the correlation between t_{prec} and E_{res} for the lower and upper limits of wave frequencies, $0.25 \Omega_{e0}$ and $0.60 \Omega_{e0}$, respectively. The color coding represents λ_{res} , with higher-energy electron scattering occurring at higher latitudes. The white dashed lines denote $\lambda_{\text{res}} = 0^\circ$ and 27° . Four energy-time dispersion curves, bounded by frequencies $0.25 \Omega_{e0}$ and $0.60 \Omega_{e0}$ and latitudes 0° and 27° , define the envelope of the precipitation flux. However, no precipitation is detected for E_k exceeding ~ 200 keV or below ~ 5 keV, since the phase space density of electrons with E_k greatly higher or lower than electron temperature (~ 20 keV) is quite low in the energy distribution. Although scattering may occur for these electrons, the resulting precipitation intensity is negligible.

Figures 2e–2h present the same quantities as Figures 2a–2d, but for the SC case. In this case, wave enhancement is prominent in 0.25 – $0.60 \Omega_{e0}$ frequency range (Figure 2f), primarily driven by nonlinear wave-particle interactions, as the frequency of maximum linear growth rate lies below $0.25 \Omega_{e0}$ and the nonlinear growth rate generally exceeds the linear one. In addition, higher-frequency waves in the range of 0.60 – $0.80 \Omega_{e0}$ are also excited after $t \sim 0.15$ s, which are likewise attributed to nonlinear effects. At $\lambda = 5^\circ$, the average wave amplitude reaches $0.008 B_{e0}$ (Figure 2e), which is 1.6 times higher than that in the TP case. The precipitation falls within the same energy range and exhibits similar energy-dispersive characteristics; however, its time duration is longer due to the additional wave excitation (Figure 2g). Moreover, since precipitation results from cumulative effect of particle scattering along the field line, even a slight increase in wave amplitude can significantly enhance precipitation intensity. In the SC case, this enhancement is most pronounced at ~ 30 – 100 keV, with the peak J_{prep} reaching $\sim 10^9$ keV/s/sr/cm 2 /MeV. To quantify this enhancement, we compare the precipitation across different energy ranges. As shown in Figure 2h, the time-averaged precipitation intensity in the 60 – 80 keV, 20 – 40 keV, and 10 – 20 keV ranges are 6.2×10^8 , 9.5×10^7 , and 3.8×10^7 keV/s/sr/cm 2 /MeV, respectively, which are 3.7, 2.0, and 1.4 times higher than the corresponding values in the TP case (1.7×10^8 , 4.9×10^7 , and 2.8×10^7 keV/s/sr/cm 2 /MeV; Figure 2d).

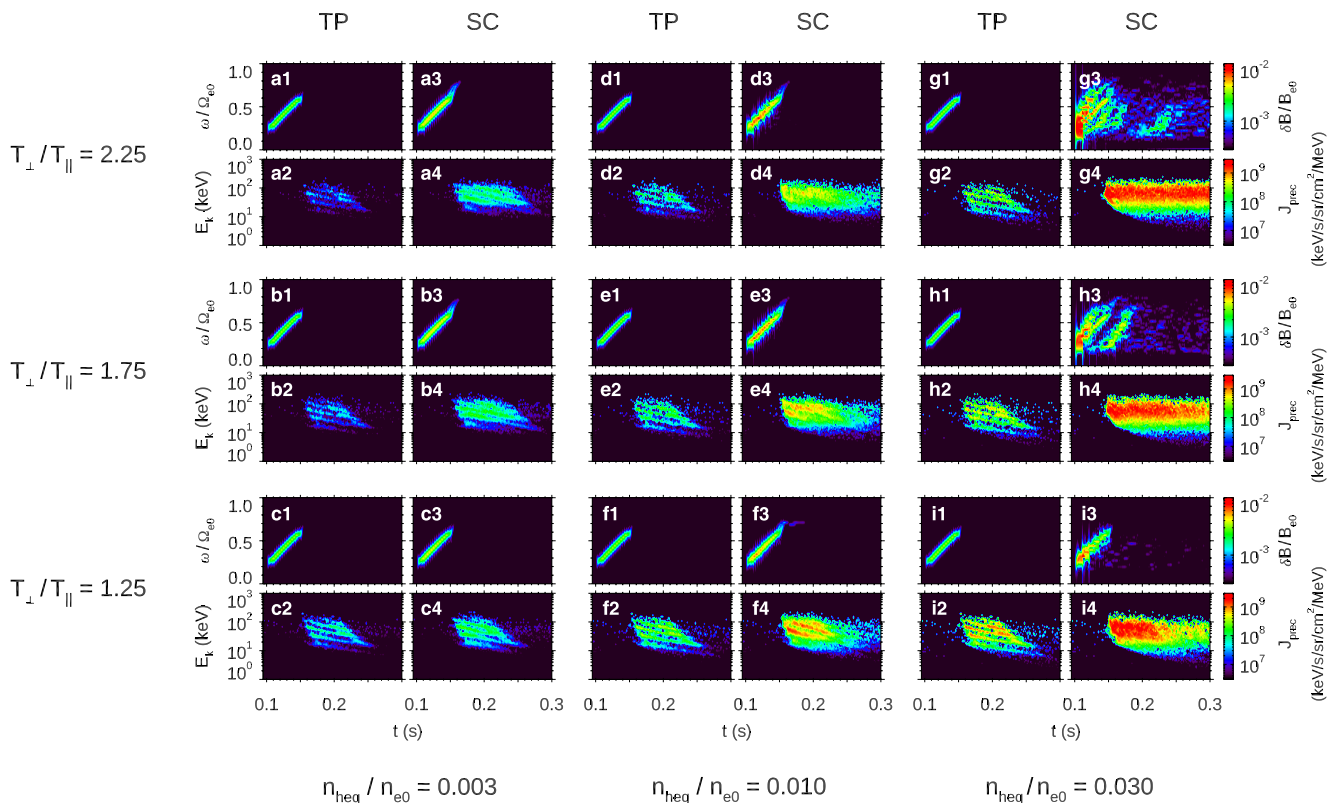


Figure 3. Parametric study of precipitation intensity as a function of n_{heq}/n_{e0} and T_{\perp}/T_{\parallel} . Chorus wave spectrum $\delta B/B_{e0}$ and electron precipitation J_{prec} at different parameters: $n_{\text{heq}}/n_{e0} = (\text{a}-\text{c}) 0.003$, $(\text{d}-\text{f}) 0.010$, and $(\text{g}-\text{i}) 0.030$, with $T_{\perp}/T_{\parallel} = (\text{a}, \text{d}, \text{g}) 2.25$, $(\text{b}, \text{e}, \text{h}) 1.75$, and $(\text{c}, \text{f}, \text{i}) 1.25$. The odd-numbered rows (even-numbered rows) present $\delta B/B_{e0}$ (J_{prec}). The odd-numbered columns (even-numbered columns) correspond to TP (SC) cases.

3.2. Parametric Study

A parametric analysis of precipitation intensity is performed by varying the equatorial number density n_{heq}/n_{e0} and the temperature anisotropy T_{\perp}/T_{\parallel} of energetic electrons. Figure 3 compares the wave amplitude $\delta B/B_{e0}$ and precipitation intensity J_{prec} between TP and SC cases for different parameter sets: $n_{\text{heq}}/n_{e0} = 0.003$, 0.010 , and 0.030 , and $T_{\perp}/T_{\parallel} = 1.25$, 1.75 , and 2.25 . In TP cases, δB remains unchanged due to the absence of particle feedback (Figures 3a1–3i1). The J_{prec} increases with n_{heq}/n_{e0} , with peak values ranging from $\sim 10^7$ to 10^8 $\text{keV/sr/cm}^2/\text{MeV}$ (Figures 3a2–3i2). In contrast, J_{prec} decreases with increasing T_{\perp}/T_{\parallel} , as the phase space density of electrons at small pitch angles is lower for larger T_{\perp}/T_{\parallel} . For a given wave amplitude, fewer particles are scattered into the loss cone. This dependence is further illustrated in Figure 4a.

For SC cases, both δB and J_{prec} increase with n_{heq}/n_{e0} . However, the dependence of J_{prec} on T_{\perp}/T_{\parallel} varies. When considering particle feedback, a larger T_{\perp}/T_{\parallel} reduces the phase space density of electrons at small pitch angles while enhancing the wave amplitude, which in turn strengthens particle scattering. The two competing effects collectively influence the precipitation flux. For small n_{heq}/n_{e0} (Figures 3a4–3f4), J_{prec} remains negatively correlated with T_{\perp}/T_{\parallel} , consistent with the TP cases. However, for larger n_{heq}/n_{e0} (Figures 3g4–3i4), J_{prec} increases with T_{\perp}/T_{\parallel} due to significant wave growth, also shown in Figure 4b. In addition, subpacket structures with amplitude modulation are formed in the SC cases, which are suggested to further enhance particle scattering (Gan et al., 2020; Tao et al., 2012).

When the free energy of energetic electrons is low (e.g., $n_{\text{heq}}/n_{e0} = 0.003$ and $T_{\perp}/T_{\parallel} = 1.25$; Figures 3c1–3c4), wave growth in SC cases is weak due to limited feedback, leading to precipitation intensities comparable with those in TP cases. As either n_{heq}/n_{e0} or T_{\perp}/T_{\parallel} increases, wave growth becomes considerable, giving rise to significant differences between two cases. The enhancement of J_{prec} is most pronounced in the tens to one hundred

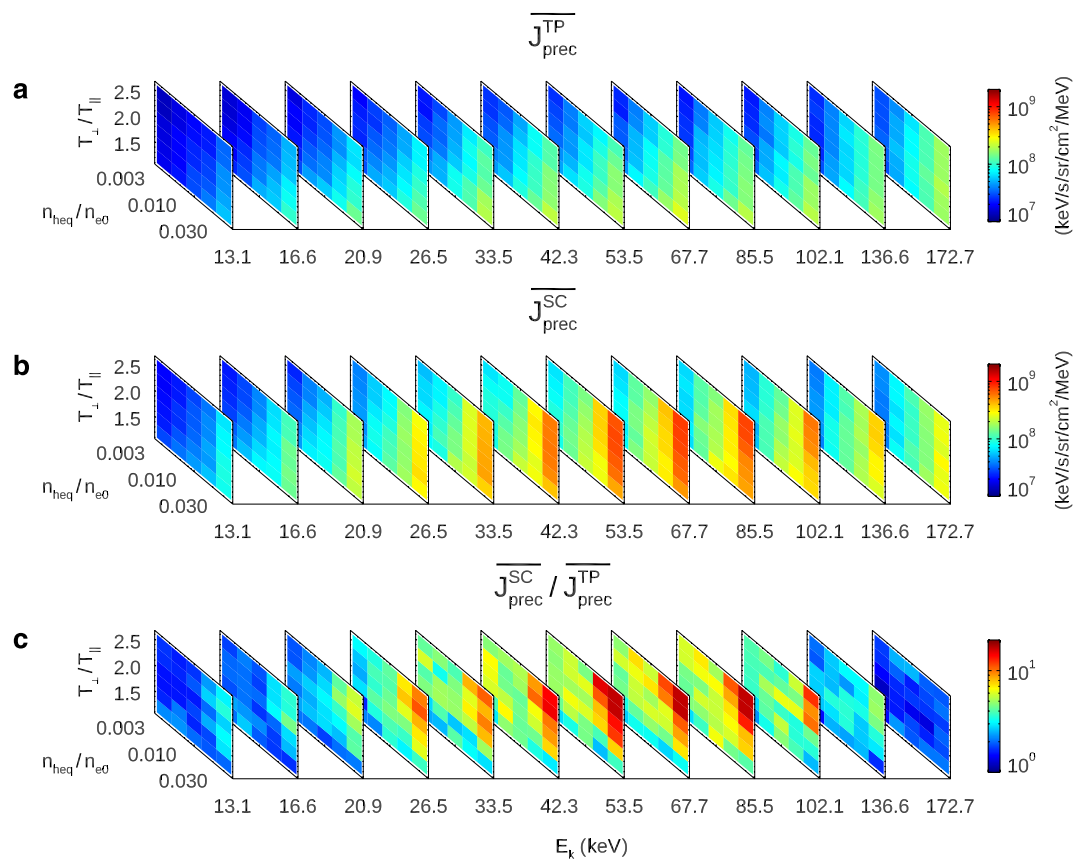


Figure 4. Quantitative comparison between TP and SC cases. (a) Time-averaged precipitation intensities $\overline{J}_{\text{prec}}^{\text{TP}}$ in TP cases and (b) $\overline{J}_{\text{prec}}^{\text{SC}}$ in SC cases as a function of n_{heq}/n_{e0} and T_{\perp}/T_{\parallel} . The slices from left to right correspond to different E_k values. (c) Ratio of $\overline{J}_{\text{prec}}^{\text{SC}} / \overline{J}_{\text{prec}}^{\text{TP}}$.

of keV range, with peak values reaching $\sim 10^8$ to 10^9 keV/s/sr/cm 2 /MeV. Notably, the J_{prec} in SC cases is comparable with the observations from the Electron Losses and Fields Investigation (ELFIN) CubeSats at an altitude of ~ 450 km, which reported $J_{\text{prec}} \sim 2 \times 10^8$ to 6×10^9 keV/s/sr/cm 2 /MeV at 63 keV (Shen et al., 2023; Zhang et al., 2022, 2023). Therefore, TP cases underestimate the precipitation intensity.

Figure 4 quantifies the differences between TP and SC cases, showing the time-averaged precipitation intensities, $\overline{J}_{\text{prec}}^{\text{TP}}$ and $\overline{J}_{\text{prec}}^{\text{SC}}$, across different energy ranges as a function of n_{heq}/n_{e0} and T_{\perp}/T_{\parallel} for (a) TP and (b) SC cases, respectively, as well as (c) their ratio $\overline{J}_{\text{prec}}^{\text{SC}} / \overline{J}_{\text{prec}}^{\text{TP}}$. In both cases, intense precipitation is concentrated within the 26.5–102.1 keV range, where SC cases exhibit an intensity nearly an order of magnitude higher than TP cases. Moreover, the difference increases with both n_{heq}/n_{e0} and T_{\perp}/T_{\parallel} , reaching a ratio of ~ 20 at $n_{\text{heq}}/n_{e0} = 0.030$ and $T_{\perp}/T_{\parallel} \geq 2$. Outside this energy range, precipitation intensity is weak, with minimal differences between TP and SC cases. These results quantitatively demonstrate that particle feedback significantly enhances electron precipitation under typical magnetospheric plasma conditions.

4. Discussion

During pitch-angle scattering, particles lose energy and transfer it for wave growth. Using the SC case shown in Figures 2e–2h, we estimate the energy contribution from precipitating electrons to chorus waves. The energy flux density S_{prec} for precipitating electrons at λ_{FT}^S is defined following Kasahara et al. (2018):

$$S_{\text{prec}} = \pi \int_{5\text{keV}}^{200\text{keV}} \frac{|\Delta E_k| \overline{J_{\text{prec}}^{\text{SC}}}}{E_k} dE_k, \quad (4)$$

where the integration is performed over $E_k = 5\text{--}200\text{ keV}$, π accounts for the area-projected-weighted loss cone (Ma et al., 2020; Mauk et al., 2017), and $\overline{J_{\text{prec}}^{\text{SC}}}$ is the time-averaged precipitation intensity as a function of E_k . Further details are presented in Figure S1 of Supporting Information S1. The S_{prec} is estimated as $1.7 \times 10^{-4} \text{ W/m}^2$.

The energy flux density of chorus waves at λ_{FT}^N is given by

$$S_{\text{wave}} = \frac{B_0|_{\lambda_{\text{FT}}^N} |\overline{\delta E} \times \overline{\delta B}|}{B_0|_{\lambda=5^\circ} \mu_0}, \quad (5)$$

where μ_0 is the vacuum permeability, $B_0|_{\lambda_{\text{FT}}^N} = 55,591 \text{ nT}$ and $B_0|_{\lambda=5^\circ} = 149 \text{ nT}$ are the background magnetic field at λ_{FT}^N and $\lambda = 5^\circ$, respectively, with the time-averaged wave electric field amplitude $\overline{\delta E} = 25 \text{ mV/m}$ and magnetic field amplitude $\overline{\delta B} = 0.72 \text{ nT}$ at $\lambda = 5^\circ$. This yield $S_{\text{wave}} = 5.3 \times 10^{-3} \text{ W/m}^2$. Therefore, precipitating electrons contribute $\sim 3\%$ ($S_{\text{prec}}/S_{\text{wave}}$) to wave growth. Note that wave energy growth arises not only from precipitating electrons but also substantially from electrons that undergo pitch-angle scattering without entering the loss cone. Moreover, precipitation intensity in our simulations is quantified under weak to moderate plasma conditions ($T_\perp/T_\parallel \sim 2$ and $n_{\text{heq}}/n_{e0} \leq 3\%$). During active geomagnetic periods, the temperature anisotropy of energetic electrons can reach $T_\perp/T_\parallel \sim 3 \text{--} 4$ (Li et al., 2009; Zhou et al., 2023), and their number density can increase to $n_{\text{heq}}/n_{e0} \sim 10\%$ (R. Chen et al., 2019; Fu et al., 2014; Li, Thorne, et al., 2011), leading to more significant feedback.

We also assess the energy contribution from precipitating electrons to wave growth using an observational event reported by Kasahara et al. (2018). Based on in situ measurements from the Arase satellite, the average precipitation intensity is $\overline{J_{\text{prec}}} \sim 2.5 \times 10^8 \text{ keV/s/sr/cm}^2/\text{MeV}$ within the 10–50 keV range, yielding an $S_{\text{prec}} = 1.9 \times 10^{-6} \text{ W/m}^2$. Given chorus wave amplitudes $\overline{\delta E} = 20 \text{ mV/m}$ and $\overline{\delta B} = 0.9 \text{ nT}$, the S_{wave} is estimated as $1.4 \times 10^{-5} \text{ W/m}^2$. This yields a $\sim 14\%$ energy contribution from precipitating electrons to wave growth, indicating non-negligible feedback.

All preceding simulations are conducted in a reduced system. We then perform simulations in the real-size magnetosphere at $L = 6$. We set $n_{\text{heq}}/n_0 = 0.001$, which is almost the lower bound of observed energetic electron number density in the magnetosphere (Gao et al., 2014), with a low temperature anisotropy of $T_\perp/T_\parallel = 1.6$. The injected wave amplitude is also reduced to $\delta B/B_{e0} = 0.003$. Other parameters are provided in Supporting Information S1. Figure 5 presents the simulation results for the (a–d) TP and (e–h) SC cases. Even with weak parameters for energetic electrons, chorus wave amplitude increases by $\sim 50\%$ (Figures 5e and 5f). This enhancement is due to the lower magnetic field curvature in the real-size magnetosphere, which favors nonlinear wave growth (Omura, 2021). Moreover, precipitation intensity shows a significant difference, with the intensity being an order of magnitude higher in the SC case compared to the TP case (Figures 5c, 5d, 5g, and 5h). This further emphasizes the importance of accounting for self-consistent wave-particle interactions when quantifying electron precipitation.

In both TP and SC cases, the differential energy flux of precipitating electrons exhibits inclined strip-like fine structures (Figures 2 and 5). We rerun the simulation cases in Figure 2 with a significantly increased ppc of 40,000 and the structures remain similar, as shown in Figure S2 of Supporting Information S1. In the real-size magnetospheric simulations, these fine structures correspond to a timescale of $\sim 0.1 \text{ s}$ at a given energy, consistent with the fast modulation ($\geq 10 \text{ Hz}$) observed in pulsating auroras (R. Chen et al., 2024; Kataoka et al., 2012; Ozaki et al., 2018). A detailed analysis of particle dynamics is necessary to investigate the underlying physics, which is beyond the scope of this study and left for future work.

Several studies have reported simultaneous observations of chorus waves and electron precipitation by highly elliptical orbit (HEO) satellites, including the Van Allen Probes (Ma et al., 2020) and Arase (Kasahara

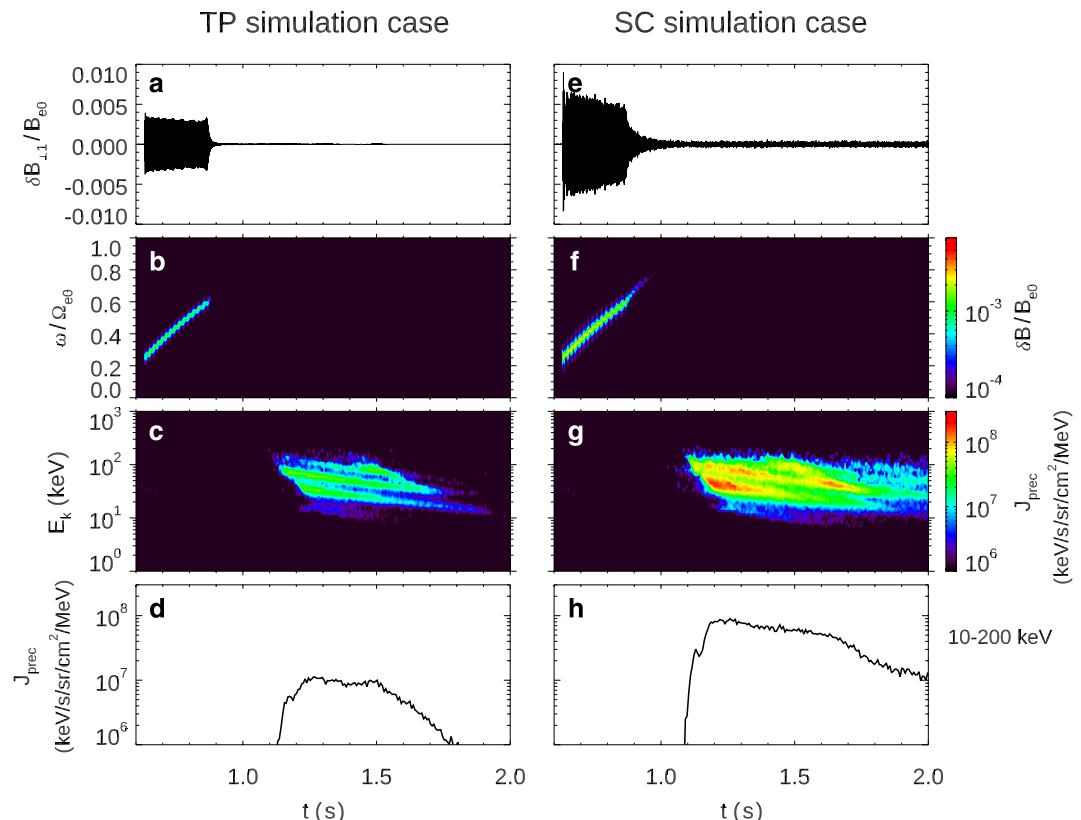


Figure 5. Simulation results of electron precipitation in the real-size magnetosphere at $L = 6$, using $n_{\text{heq}}/n_{e0} = 0.001$ and $T_{\perp}/T_{\parallel} = 1.60$ for energetic electrons. (a, e) Chorus waveform and (b, f) spectrum at $\lambda = 5^\circ$. (c, g) Differential precipitating energy flux J_{prec} at λ_{FT}^S . (d, h) Temporal evolution of the average J_{prec} for $E_k = 10\text{--}200 \text{ keV}$. Left: TP case; Right: SC case.

et al., 2018). These observations capture localized precipitation at latitudes coincident with chorus waves, while the present study focuses on precipitation at ionospheric altitudes. We have made efforts to validate our simulation results from observational data. The simulation parameters are selected to reflect typical observational values. The energy range and the energy-dispersive characteristics of the simulated precipitation are consistent with satellite measurements. Parametric analysis further indicates that precipitation intensities in the SC cases are comparable to observed values. A direct one-to-one comparison between simulation and observation remains challenging because HEO observations generally capture wave properties at a single location, whereas low-altitude precipitation reflects the integrated effect along the entire magnetic field line. Quantifying the ratio $J_{\text{prec}}/J_{\text{trap}}$ provides a practical method for comparing simulations with LEO satellite observations, where J_{trap} represents the differential energy flux of trapped particles. It should be noted, however, that J_{trap} varies with latitude because the mirror points of trapped particles depend on pitch angle. Detailed comparisons between simulations and observations are left for future work.

5. Summary

In this study, we quantify electron precipitation driven by chorus waves in a dipole field through SC simulations, using typical plasma parameters at $L \sim 6$. It is found that electrons with energies ranging from ~ 10 to 200 keV are precipitated, and their energy flux exhibits energy-dispersive characteristics. The precipitation intensity J_{prec} reaches $\sim 10^8\text{--}10^9 \text{ keV/s/sr/cm}^2/\text{MeV}$, consistent with observations from satellites at ionospheric altitudes (Shen et al., 2023; Zhang et al., 2022, 2023). Parametric analysis indicates that J_{prec} generally increases with the number density of energetic electrons n_{heq}/n_{e0} and decreases with the temperature anisotropy T_{\perp}/T_{\parallel} . However, for large n_{heq}/n_{e0} , J_{prec} becomes positively correlated with T_{\perp}/T_{\parallel} due to significant wave growth.

As a comparison, TP simulations underestimate the precipitation intensity by nearly an order of magnitude, primarily in the ~26.5–102.1 keV range, where intense precipitation occurs. At other energy ranges, the intensity is weak and is comparable to that in SC simulations. These results highlight the necessity of self-consistent wave-particle interactions for quantifying electron precipitation.

Conflict of Interest

The authors declare no conflicts of interest relevant to this study.

Data Availability Statement

The data used to reproduce the figures in this manuscript are publicly available at H. Chen (2025).

Acknowledgments

This work was supported by the NASA Grant 80NSSC21K1688 and the NSF Grant AGS-2453814. LC was supported by the NSF Grant AGS-2225121. YO and YH were supported by JSPS KAKENHI Grants JP20H01960 and JP23H05429.

References

- Anderson, K. A., & Milton, D. W. (1964). Balloon observations of X rays in the auroral zone: 3. High time resolution studies. *Journal of Geophysical Research*, 69(21), 4457–4479. <https://doi.org/10.1029/JZ069i021p04457>
- Artemyev, A. V., Zhang, X.-J., Zou, Y., Mourenas, D., Angelopoulos, V., Vainchtein, D., et al. (2022). On the nature of intense sub-relativistic electron precipitation. *Journal of Geophysical Research: Space Physics*, 127(6), e2022JA030571. <https://doi.org/10.1029/2022JA030571>
- Bortnik, J., Thorne, R. M., & Inan, U. S. (2008). Nonlinear interaction of energetic electrons with large amplitude chorus. *Geophysical Research Letters*, 35(21), L21102. <https://doi.org/10.1029/2008GL035500>
- Breneman, A. W., Crew, A., Sample, J., Klumpar, D., Johnson, A., Agapitov, O., et al. (2017). Observations directly linking relativistic electron microbursts to whistler mode chorus: Van Allen Probes and FIREBIRD II. *Geophysical Research Letters*, 44(22), 11265–11272. <https://doi.org/10.1002/2017GL075001>
- Burtis, W. J., & Helliwell, R. A. (1969). Banded chorus a new type of VLF radiation observed in the magnetosphere by OGO 1 and OGO 3. *Journal of Geophysical Research*, 74(11), 3002–3010. <https://doi.org/10.1029/JA074i011p03002>
- Chen, H. (2025). Database of “Quantifying electron precipitation driven by chorus waves using self-consistent particle-in-cell simulations” [Dataset]. Zenodo. <https://doi.org/10.5281/zenodo.15161490>
- Chen, H., Wang, X., Chen, L., Omura, Y., Lu, Q., Chen, R., et al. (2023). Simulation of downward frequency chirping in the rising tone chorus element. *Geophysical Research Letters*, 50(9), e2023GL103160. <https://doi.org/10.1029/2023GL103160>
- Chen, H., Wang, X., Chen, L., Omura, Y., Tsurutani, B. T., Lin, Y., & Xia, Z. (2023). Evolution of chorus subpackets in the Earth's magnetosphere. *Geophysical Research Letters*, 50(21), e2023GL105938. <https://doi.org/10.1029/2023GL105938>
- Chen, H., Wang, X., Chen, L., Omura, Y., Miyoshi, Y., et al. (2025). Simulation study of chorus wave modulation and associated electron precipitation. *Geophysical Research Letters*, 52, e2025GL118562. <https://doi.org/10.1029/2025GL118562>
- Chen, L., Breneman, A. W., Xia, Z., & Zhang, X.-J. (2020). Modeling of bouncing electron microbursts induced by ducted chorus waves. *Geophysical Research Letters*, 47(17), e2020GL089400. <https://doi.org/10.1029/2020GL089400>
- Chen, R., Gao, X., Lu, Q., & Wang, S. (2019). Unraveling the correlation between chorus wave and electron beam-like distribution in the Earth's magnetosphere. *Geophysical Research Letters*, 46(21), 11671–11678. <https://doi.org/10.1029/2019GL085108>
- Chen, R., Miyoshi, Y., Gao, X., Lu, Q., Tsurutani, B. T., Hosokawa, K., et al. (2024). Observational evidence for three time-scale modulations in the pulsating aurora. *Geophysical Research Letters*, 51(16), e2024GL108253. <https://doi.org/10.1029/2024GL108253>
- Fu, X., Cowee, M. M., Friedel, R. H., Funsten, H. O., Gary, S. P., Hospodarsky, G. B., et al. (2014). Whistler anisotropy instabilities as the source of banded chorus: Van Allen Probes observations and particle-in-cell simulations. *Journal of Geophysical Research: Space Physics*, 119(10), 8288–8298. <https://doi.org/10.1002/2014JA020364>
- Gan, L., Li, W., Ma, Q., Albert, J. M., Artemyev, A. V., & Bortnik, J. (2020). Nonlinear interactions between radiation belt electrons and chorus waves: Dependence on wave amplitude modulation. *Geophysical Research Letters*, 47(4), e2019GL085987. <https://doi.org/10.1029/2019GL085987>
- Gao, X., Li, W., Thorne, R. M., Bortnik, J., Angelopoulos, V., Lu, Q., et al. (2014). New evidence for generation mechanisms of discrete and hiss-like whistler mode waves. *Geophysical Research Letters*, 41(14), 4805–4811. <https://doi.org/10.1002/2014GL060707>
- Gao, X., Ma, J., Shao, T., Chen, R., Ke, Y., & Lu, Q. (2023). Why chorus waves are the dominant driver for diffuse auroral precipitation. *Science Bulletin*, 69(5), 597–600. <https://doi.org/10.1016/j.scib.2023.12.009>
- Hikishima, M., Omura, Y., & Summers, D. (2010). Microburst precipitation of energetic electrons associated with chorus wave generation. *Geophysical Research Letters*, 37(7), L07103. <https://doi.org/10.1029/2010GL042678>
- Horne, R. B., & Thorne, R. M. (1998). Potential waves for relativistic electron scattering and stochastic acceleration during magnetic storms. *Geophysical Research Letters*, 25(15), 3011–3014. <https://doi.org/10.1029/98GL01002>
- Jaynes, A. N., Lessard, M. R., Takahashi, K., Ali, A. F., Malaspina, D. M., Michell, R. G., et al. (2015). Correlated Pc4–5 ULF waves, whistler-mode chorus, and pulsating aurora observed by the Van Allen Probes and ground-based systems. *Journal of Geophysical Research: Space Physics*, 120(10), 8749–8761. <https://doi.org/10.1002/2015JA021380>
- Kang, N., Bortnik, J., Zhang, X., Claudepierre, S., & Shi, X. (2022). Relativistic microburst scale size induced by a single point-source chorus element. *Geophysical Research Letters*, 49(23), e2022GL100841. <https://doi.org/10.1029/2022GL100841>
- Kasahara, S., Miyoshi, Y., Yokota, S., Mitani, T., Kasahara, Y., Matsuda, S., et al. (2018). Pulsating aurora from electron scattering by chorus waves. *Nature*, 554(7692), 337–340. <https://doi.org/10.1038/nature25505>
- Kataoka, R., Miyoshi, Y., Hampton, D., Ishii, T., & Kozako, H. (2012). Pulsating aurora beyond the ultra-low-frequency range. *Journal of Geophysical Research*, 117(A8), A08336. <https://doi.org/10.1029/2012JA017987>
- Ke, Y., Lu, Q., Gao, X., Chen, H., & Chen, R. (2022). Ray-tracing simulations of whistler-mode wave propagation in different rescaled dipole magnetic fields. *Earth Planetary Physics*, 6(6), 555–562. <https://doi.org/10.26464/epp2022048>
- Khazanov, G. V., Robinson, R. M., Zesta, E., Sibeck, D. G., Chu, M., & Grubbs, G. A. (2018). Impact of precipitating electrons and magnetosphere-ionosphere coupling processes on ionospheric conductance. *Space Weather*, 16(7), 829–837. <https://doi.org/10.1029/2018SW001837>

- Kong, Z., Gao, X., Lu, Q., Lei, W., Wang, X., Ma, J., et al. (2025). Modulation of electron precipitation regulated by electron injection: PIC simulations. *Physics of Plasmas*, 32(2), 022108. <https://doi.org/10.1063/5.0241061>
- Li, W., Bortnik, J., Thorne, R. M., Nishimura, Y., Angelopoulos, V., & Chen, L. (2011). Modulation of whistler mode chorus waves: 2. Role of density variations. *Journal of Geophysical Research*, 116(A6), A06206. <https://doi.org/10.1029/2010JA016313>
- Li, W., Thorne, R. M., Angelopoulos, V., Bonnell, J. W., McFadden, J. P., Carlson, C. W., et al. (2009). Evaluation of whistler-mode chorus intensification on the nightside during an injection event observed on the THEMIS spacecraft. *Journal of Geophysical Research*, 114(A1), A00C14. <https://doi.org/10.1029/2008JA013554>
- Li, W., Thorne, R. M., Bortnik, J., Nishimura, Y., & Angelopoulos, V. (2011). Modulation of whistler mode chorus waves: 1. Role of compressional Pe4–5 pulsations. *Journal of Geophysical Research*, 116(A6), A06205. <https://doi.org/10.1029/2010JA016312>
- Lu, Q., Chen, L., Wang, X., Gao, X., Lin, Y., & Wang, S. (2021). Repetitive emissions of rising-tone chorus waves in the inner magnetosphere. *Geophysical Research Letters*, 48(15), e2021GL094979. <https://doi.org/10.1029/2021GL094979>
- Lu, Q., Ke, Y., Wang, X., Liu, K., Gao, X., Chen, L., & Wang, S. (2019). Two-dimensional general curvilinear particle-in-cell (gcPIC) simulation of rising-tone chorus waves in a dipole magnetic field. *Journal of Geophysical Research: Space Physics*, 124(6), 4157–4167. <https://doi.org/10.1029/2019ja026586>
- Lyons, L. R. (1992). Formation of auroral arcs via magnetosphere-ionosphere coupling. *Reviews of Geophysics*, 30(2), 93–112. <https://doi.org/10.1029/92RG00002>
- Ma, Q., Connor, H. K., Zhang, X.-J., Li, W., Shen, X.-C., Gillespie, D., et al. (2020). Global survey of plasma sheet electron precipitation due to whistler mode chorus waves in Earth's magnetosphere. *Geophysical Research Letters*, 47(15), e2020GL088798. <https://doi.org/10.1029/2020GL088798>
- Macúšová, E., Santolík, O., Décréau, P., Demekhov, A. G., Nunn, D., Gurnett, D. A., et al. (2010). Observations of the relationship between frequency sweep rates of chorus wave packets and plasma density. *Journal of Geophysical Research*, 115, A12257. <https://doi.org/10.1029/2010JA015468>
- Mauk, B. H., Haggerty, D. K., Paranicas, C., Clark, G., Kollmann, P., Rymer, A. M., et al. (2017). Juno observations of energetic charged particles over Jupiter's polar regions: Analysis of monodirectional and bidirectional electron beams. *Geophysical Research Letters*, 44(10), 4410–4418. <https://doi.org/10.1002/2016GL072286>
- Miyoshi, Y., Katoh, Y., Nishiyama, T., Sakanoi, T., Asamura, K., & Hirahara, M. (2010). Time of flight analysis of pulsating aurora electrons, considering wave-particle interactions with propagating whistler mode waves. *Journal of Geophysical Research*, 115(A10), A10312. <https://doi.org/10.1029/2009JA015127>
- Miyoshi, Y., Oyama, S., Saito, S., Kurita, S., Fujiwara, H., Kataoka, R., et al. (2015). Energetic electron precipitation associated with pulsating aurora: EISCAT and Van Allen Probes observations. *Journal of Geophysical Research: Space Physics*, 120(4), 2754–2766. <https://doi.org/10.1002/2014ja020690>
- Miyoshi, Y., Saito, S., Kurita, S., Asamura, K., Hosokawa, K., Sakanoi, T., et al. (2020). Relativistic electron microbursts as high-energy tail of pulsating aurora electrons. *Geophysical Research Letters*, 47(21), e2020GL090360. <https://doi.org/10.1029/2020GL090360>
- Mozer, F. S., Agapitov, O. V., Blake, J. B., & Vasko, I. Y. (2018). Simultaneous observations of lower band chorus emissions at the equator and microburst precipitating electrons in the ionosphere. *Geophysical Research Letters*, 45(2), 511–516. <https://doi.org/10.1002/2017GL076120>
- O'Brien, T. P., Lemon, C. L., & Blake, J. B. (2022). Electron precipitation curtains—Simulating the microburst origin hypothesis. *Journal of Geophysical Research: Space Physics*, 127(8), e2022JA030370. <https://doi.org/10.1029/2022JA030370>
- Omura, Y. (2021). Nonlinear wave growth theory of whistler-mode chorus and hiss emissions in the magnetosphere. *Earth Planets and Space*, 73(1), 1–28. <https://doi.org/10.1186/s40623-021-01380w>
- Ozaki, M., Miyoshi, Y., Shiokawa, K., Hosokawa, K., Oyama, S. I., Kataoka, R., et al. (2019). Visualization of rapid electron precipitation via chorus element wave-particle interactions. *Nature Communications*, 10(1), 257. <https://doi.org/10.1038/s41467-018-07996-z>
- Ozaki, M., Shiokawa, K., Miyoshi, Y., Hosokawa, K., Oyama, S., Yagitani, S., et al. (2018). Microscopic observations of pulsating aurora associated with chorus element structures: Coordinated Arase satellite-PWING observations. *Geophysical Research Letters*, 45(22), 12125–12134. <https://doi.org/10.1029/2018GL079812>
- Saito, S., Miyoshi, Y., & Seki, K. (2012). Relativistic electron microbursts associated with whistler chorus rising tone elements: GEMSIS-RBW simulations. *Journal of Geophysical Research*, 117(A10), A10206. <https://doi.org/10.1029/2012JA018020>
- Shen, X.-C., Li, W., Capannolo, L., Ma, Q., Qin, M., Artemyev, A. V., et al. (2023). Modulation of energetic electron precipitation driven by three types of whistler mode waves. *Geophysical Research Letters*, 50(8), e2022GL101682. <https://doi.org/10.1029/2022GL101682>
- Summers, D., Ni, B., & Meredith, N. P. (2007). Timescales for radiation belt electron acceleration and loss due to resonant wave-particle interactions: 2. Evaluation for VLF chorus, ELF hiss, and electromagnetic ion cyclotron waves. *Journal of Geophysical Research*, 112(A4), A04207. <https://doi.org/10.1029/2006JA011993>
- Tao, X., Bortnik, J., Thorne, R. M., Albert, J. M., & Li, W. (2012). Effects of amplitude modulation on nonlinear interactions between electrons and chorus waves. *Geophysical Research Letters*, 39(6), L06102. <https://doi.org/10.1029/2012GL051202>
- Tsurutani, B. T., Lakhina, G. S., & Verkhoglyadova, O. P. (2013). Energetic electron (>10 keV) microburst precipitation, 5–15 s X-ray pulsations, chorus, and wave-particle interactions: A review. *Journal of Geophysical Research: Space Physics*, 118(5), 2296–2312. <https://doi.org/10.1002/jgra.50264>
- Tsurutani, B. T., & Smith, E. J. (1974). Postmidnight chorus: A substorm phenomenon. *Journal of Geophysical Research*, 79(1), 118–127. <https://doi.org/10.1029/JA079i001p00118>
- Wang, X., Chen, H., Omura, Y., Hsieh, Y. K., Chen, L., Lin, Y., et al. (2024). Resonant electron signatures in the formation of chorus wave subpackets. *Geophysical Research Letters*, 51(8), e2023GL108000. <https://doi.org/10.1029/2023GL108000>
- Yue, C., An, X., Bortnik, J., Ma, Q., Li, W., Thorne, R. M., et al. (2016). The relationship between the macroscopic state of electrons and the properties of chorus waves observed by the Van Allen Probes. *Geophysical Research Letters*, 43(15), 7804–7812. <https://doi.org/10.1002/2016GL070084>
- Zhang, B., Lotko, W., Brambles, O., Wiltberger, M., & Lyon, J. (2015). Electron precipitation models in global magnetosphere simulations. *Journal of Geophysical Research: Space Physics*, 120(2), 1035–1056. <https://doi.org/10.1002/2014JA020615>
- Zhang, X.-J., Angelopoulos, V., Artemyev, A., Mourenas, D., Agapitov, O., Tsai, E., & Wilkins, C. (2023). Temporal scales of electron precipitation driven by whistler-mode waves. *Journal of Geophysical Research: Space Physics*, 128(1), e2022JA031087. <https://doi.org/10.1029/2022JA031087>
- Zhang, X.-J., Angelopoulos, V., Mourenas, D., Artemyev, A., Tsai, E., & Wilkins, C. (2022). Characteristics of electron microburst precipitation based on high-resolution ELFIN measurements. *Journal of Geophysical Research: Space Physics*, 127(5), e2022JA030509. <https://doi.org/10.1029/2022JA030509>

Zhou, X., Gao, X., Chen, R., Lu, Q., Ke, Y., Ma, J., & Kong, Z. (2023). Direct observation of rising-tone chorus triggered by enhanced solar wind pressure. *Journal of Geophysical Research: Space Physics*, 128(11), e2023JA031787. <https://doi.org/10.1029/2023JA031787>

References From the Supporting Information

- Bortnik, J., Inan, U. S., & Bell, T. F. (2006). Landau damping and resultant unidirectional propagation of chorus waves. *Geophysical Research Letters*, 33(3), L03102. <https://doi.org/10.1029/2005GL024553>
- Chen, H., Wang, X., Zhao, H., Lin, Y., Chen, L., Omura, Y., et al. (2024). Electron dynamics associated with advection and diffusion in self-consistent wave-particle interactions with oblique chorus waves. *Geophysical Research Letters*, 51(14), e2024GL110362. <https://doi.org/10.1029/2024GL110362>
- Li, W., Bortnik, J., Thorne, R. M., Cully, C. M., Chen, L., Angelopoulos, V., et al. (2013). Characteristics of the Poynting flux and wave normal vectors of whistler-mode waves observed on THEMIS. *Journal of Geophysical Research: Space Physics*, 118(4), 1461–1471. <https://doi.org/10.1002/jgra.50176>
- Nogi, T., Nakamura, S., & Omura, Y. (2020). Full particle simulation of whistler-mode triggered falling-tone emissions in the magnetosphere. *Journal of Geophysical Research: Space Physics*, 125(10), e2020JA027953. <https://doi.org/10.1029/2020JA027953>